Chapter 7
Self-Healing of Mechanical Properties: Evaluation by Tensile Testing

In this Section the evaluation of the mechanical consequences of self-healing is discussed. In particular, the recovery of such mechanical properties as stiffness is addressed. The tensile testing of self-healing composites with different types of fibers are analyzed in Sects. 7.1 and 7.2. Fatigue testing under a static loads is discussed in Sect. 7.3. The case of increasing stresses and the effect of self-healing features on crack propagation are described in Sect. 7.4.

7.1 Tensile Testing: Stiffness Recovery in Composites with Co-electrospun Polyacrylonitrile–DMS Resin Monomer–Curing Agent Nanofibers

For the tensile testing of self-healing nanofiber (NF) mats and/or composites incorporating such mats, specimens are typically shaped as rectangular in shape; sometimes the dog-bone shape is used. Self-healing polyacrylonitrile (PAN)–DMS resin monomer–curing agent (PRC) NF mats formed by Lee et al. (2015) by co-electrospinning, as described in Sect. 4.2, were used to fabricate NF-reinforced composites with different matrices. To prepare composite specimens for tensile testing, both the non-self-healing monolithic PAN (used for comparison) and self-healing core-shell PRC NF mats were cut into specimens with dimensions of $\ell_0 \times w_0 =$ 90 mm $\times$ 23 mm (cf. Fig. 7.1a). These sections were sandwiched as middle layer between polydimethylsiloxane (PDMS, using pre-mixed resin monomer and curing agent at a ratio of 10:1) layers. The resulting PDMS-encased composites were cured at room temperature for 24 h. These specimens were subsequently used in tensile testing (see Fig. 7.1b). The initial thickness t_0 of each specimen was measured ten times using micrometer and the average of the ten measurements was recorded. The values of t_0 for the PAN and PRC NF-reinforced composites were 0.485 mm and 0.425 mm, respectively. Such layered composites present significant interest as self-

A. L. Yarin et al., *Self-Healing Nanotextured Vascular Engineering Materials*, Advanced Structured Materials 105, https://doi.org/10.1007/978-3-030-05267-6_7

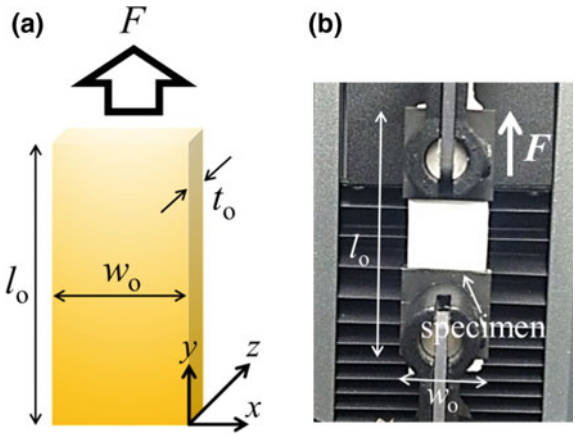

Fig. 7.1 **a** Specimen schematic and **b** photograph of apparatus for tensile testing. Reprinted with permission from Lee et al. (2015)

healing adhesive layers at ply surfaces in laminate composites (cf. Sects. 6.6 and 8.4); thus, mechanical testing of thin specimens was attempted.

The PDMS matrices of the prepared composites can be damaged and develop multiple microcracks during the stretching of such specimens, as occurs in the matrices of many other composites used in aerospace and other industries. However, in the present case, the PDMS matrices are embedded with mutually entangled core-shell NFs containing resin monomer and curing agent in their cores. These NFs are also damaged during stretching. Upon damage, they release resin monomer and curing agent into the surrounding microcracks of the PDMS matrix. Polymerization of the released resin in the presence of curing agent then occurs, and PDMS stitches spanning the banks of microcracks in the PDMS matrix are formed (see Sect. 3.4). This is the self-healing mechanism examined using tensile testing.

The first goal of any tensile test is to quantify the elastic behavior of the materials, as characterized by Hooke's law with the two material parameters of Young's modulus E and Poisson's ratio ν; all other elastic parameters used can be expressed using E and ν (Landau and Lifshitz 1986). In the tensile tests described below, only the specimen edges are loaded by the two pulling grips, whereas all the other sides are unloaded. Under such conditions, Hooke's law is reduced to the most elementary form:

$$\sigma_{xx} = E\varepsilon_{xx} \tag{7.1}$$

irrespective of the value of ν; σ_{xx} and ε_{xx} are the tensile stress and strain, with x being the stretching direction. Note that the value of E characterizes the specimen stiffness.

The PDMS-encased composite specimens were tensile tested by Lee et al. (2015) using an Instron 5942 machine. The initial specimen length (gauge length) between the upper and lower grips is set to 20 mm (cf. Fig. 7.1b). During the experiments, the stretching rate was 1 mm/min. Such low stretching rates are characteristic of many industrial applications, where the accumulation of mechanically generated

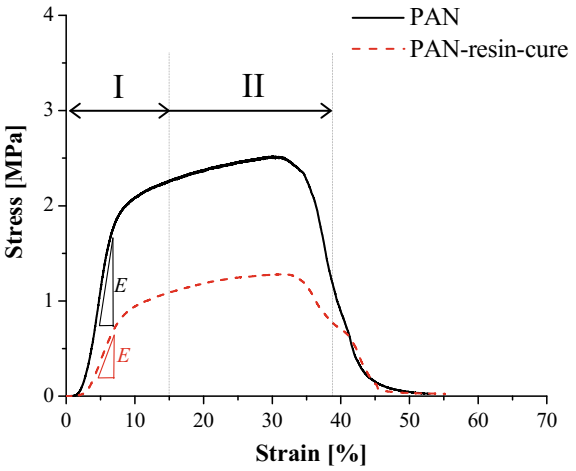

Fig. 7.2 Stress–strain curves measured in tensile testing of the PAN and PRC NF mats. Reprinted with permission from Lee et al. (2015)

microcracks occurs relatively slowly before suddenly causing a catastrophic event. The acquired data were presented as the stress–strain curves.

The procedure described below was used to evaluate the self-healing features of the PDMS-encased specimens containing the self-healing

core-shell PRC NFs. The specimens were stretched to strains of 15–18%, which caused internal damage. The accumulated damage at such strains was revealed during the experiments on the PDMS-encased specimens containing non-self-healing PAN NFs. These specimens did not recover their original stress–strain curves, as discussed below. The tested PDMS-encased specimens with self-healing core-shell PRC NFs were left for 24 h to ensure that polymerization occurred between the released resin monomer and curing agent from the damaged NFs. Subsequently, the self-healing specimens were further analyzed by tensile testing to evaluate the degree of recovery of their pre-damage stress–strain curves, wherein recovery would imply full self-healing.

Figure 7.2 shows the tensile test results for both PAN and self-healing PRC NF mats. The thicknesses of the PAN and PRC fiber mats are 0.089 mm and 0.191 mm, respectively; the PRC mat is 2.15 times thicker than the PAN mat. This is because the two additional components (dimethyl siloxane or DMS resin monomer and curing agent; cf. Sect. 2.2) were simultaneously supplied to the PAN solution during the co-electrospinning process (see Sect. 4.2). The Young's moduli E of the PAN NF mat and the self-healing PRC NF mat are measured as the slopes of the linear portions of the stress–strain curves in Fig. 7.2, according to Eq. (7.1). They are 46.45 MPa and 18.05 MPa for the PAN and self-healing PRC NF mats, respectively. This indicates that the fully solidified PAN NF mat is stiffer than the self-healing PRC NF mat containing liquid resin monomer or curing agent within the NF cores. The ultimate tensile strength of the PAN NF mat is also twice that of the self-healing PRC NF mat.

The results reveal two recognizable well-defined regimes of deformation within the stress–strain curves. In the elastic regime I, the stress-strain dependences are

initially linear and then, plasticity sets in; the intermediate plastic regime II, the dependences are non-linear; these initially regimes are followed by ultimate catastrophic failure. The regimes are typical for the different NF mats (Khansari et al. 2012; 2013, Sinha-Ray et al. 2012, 2014; Yarin et al. 2014).

Figure 7.3 shows the results of repeated tensile testing at strains reaching 15% (including the elastic regime I and the initial part of the plastic regime II) for both the PAN and PRC NF mats. Stretching to 15% (deep into the irreversible plastic regime) causes moderate damage to the mats. Each mat is initially stretched and then allowed "resting" for 24 h before the sequential tensile tests. Each mat was subjected to four sequential tensile tests. Figure 7.3a reveals that the PAN NF mat is deteriorating in its mechanical properties immediately after the first tensile test. During the second tensile test, the stress–strain curve shows catastrophic failure at the strain of 7.5%. During the sequential tensile tests, the PAN mat exhibits only a slight resistance to stretching; its stiffness and ultimate strength significantly decline during the sequential tests. On the contrary, the self-healing PRC specimen shows similar stress–strain curves for the four sequential tensile tests (cf. Fig. 7.3b). In Fig. 7.3c, the Young's moduli measured during the sequential tests are normalized by that obtained during the first test. The trends for the PAN mat and the self-healing PRC mat are drastically different. During the fourth sequential tensile tests, the Young's moduli are decreased (relative to the original values) by 90% for the PAN mat, but only by 30% for the self-healing PRC specimen. Specifically, the specimen healed over the rest time of 24 h by the release of the resin monomer and curing agent that were stored separately within the NF cores. It should be emphasized that the PAN NF mat is weakened significantly during the sequential tests and completely failed during the fourth tensile test, unlike the self-healing PRC mat, as shown in Fig. 7.3d.

In addition to the sequential tensile tests up to the strain of 15%, as illustrated in Fig. 7.3, similar tests are conducted by stretching the mats up to the level related to catastrophic failure (30% strain). The corresponding results are presented in Fig. 7.4. As Fig. 7.4d illustrates, during these tests, the stretched fiber mats shrink significantly in the middle unlike those shown in Fig. 7.3d. It should be emphasized that the specimens shown in Figs. 7.3d and 7.4d undergo different strain regimes. The specimens shown in Fig. 7.3d experience repeated stretching in the moderate strain range (regime I, strains ε_{xx} reaching 15%), whereas those shown in Fig. 7.4d are stretched beyond failure (regime II, strains ε_{xx} reaching 30%). The plastic deformation in regime II yields the dog-bone shape in the middle of the mats, characteristic of many materials in such situations.

Notably, the self-healing PRC mat shows behavior similar to that of the PAN specimen (see Fig. 7.4a and b). The self-healing mat only slightly outperforms the pure PAN specimen, as shown in Fig. 7.4c. Indeed, the normalized Young's moduli for the self-healing PRC material are only 11% and 15% greater than those of the pure PAN specimen during the second and third tensile tests, respectively. The experimental results for extensive sequential stretching imply that the ruptured NF sections are separated to such an extent that self-healing becomes practically impossible, despite the release of both resin monomer and curing agent from the cores of the ruptured NFs.

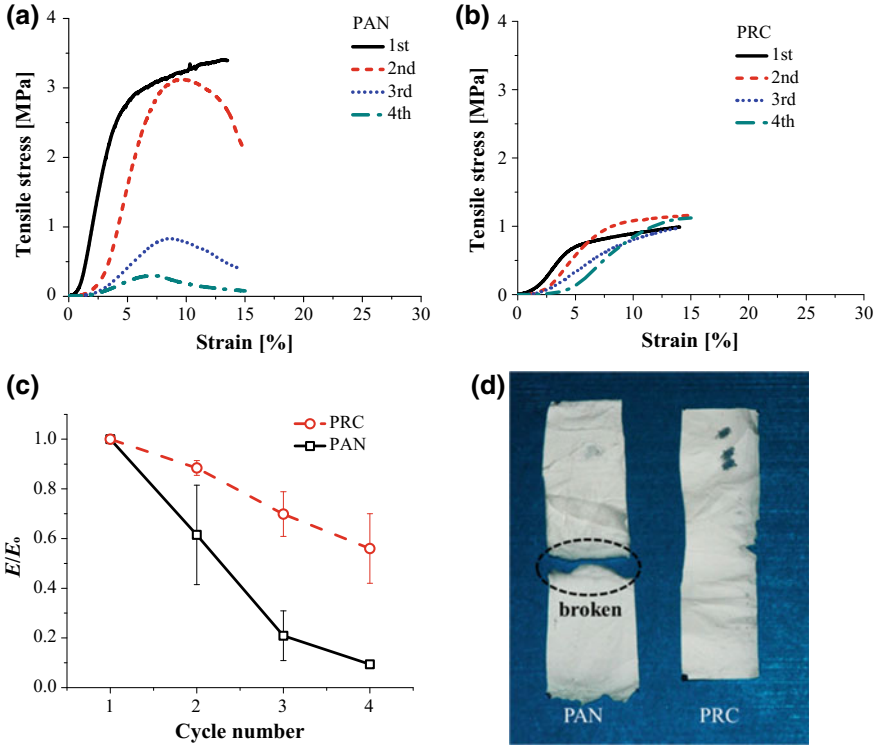

Fig. 7.3 Stress–strain curves measured during tensile tests with strain reaching 15% (elastic regime and the initial part of the plastic regime). **a** PAN NF mat, **b** PRC NF mat. **c** Relative variation in Young's modulus values during sequential tests; the Young's modulus measured during the first stretching is denoted E_0, while those measured during the sequential stretching tests of the same mat are denoted E. **d** Photographs of the specimens following the sequential tensile tests. Reprinted with permission from Lee et al. (2015)

Now the results of tensile testing for the corresponding composite specimens are considered. The PDMS-impregnated composite specimen with the self-healing PRC NFs were subjected to tensile tests every 24 h to strains of 15–18%. Figure 7.5 shows that the relative values of the ratio E/E_0 for the PRC composite specimens differ from those of both pure PDMS and the PAN-PRC-based composite specimens. The pure PDMS specimens are used as references; their Young's moduli are relatively unchanged over the four sequential tensile tests. This correlates with the results of the previous research (Kim et al. 2011), where the stress–strain curve of a PDMS specimen stretched to the 50% strain after ten tests is similar to the initial curve. In general, PDMS is regarded as a good elastomer.

Figure 7.5d shows that the stiffness of the PDMS composite with self-healing PRC fibers is not sustained, but enhanced following the sequential tensile tests. Indeed, after the fourth test, the Young's modulus of the composite is increased by a factor of

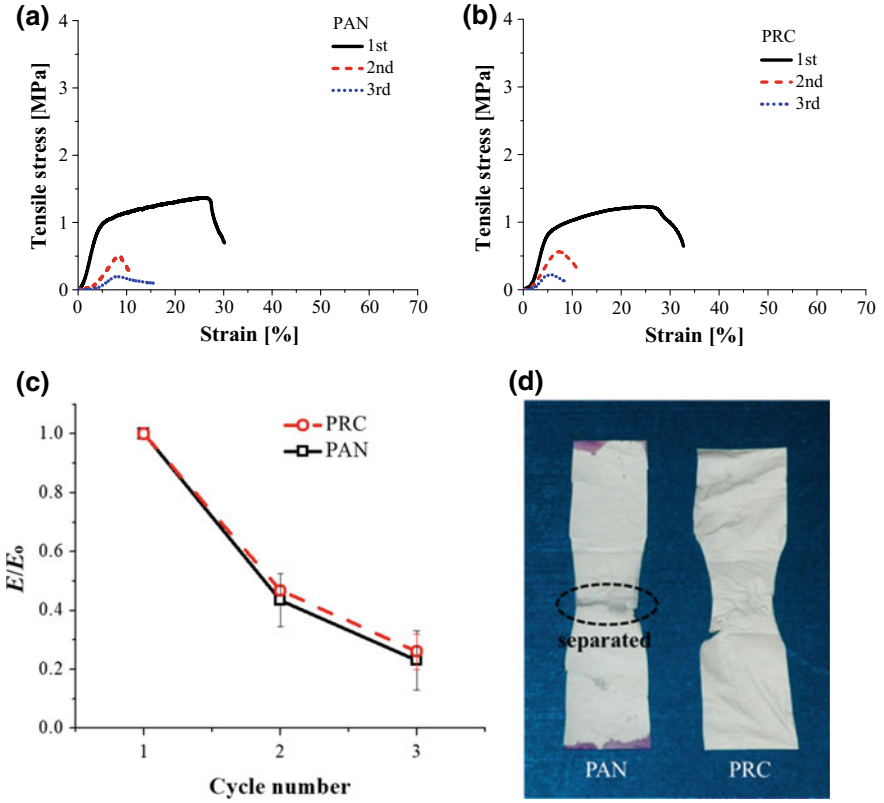

Fig. 7.4 Stress–strain curves measured during tensile tests to 30% strain (catastrophic failure regime). **a** PAN NF mat, **b** PRC NF mat. **c** Relative variation of the Young's moduli during the sequential tests; the Young's modulus measured during the first stretching is denoted E_0, while those measured during the sequential stretching tests of the same mat are denoted E. **d** Photographs of the specimens following the sequential tensile tests. Reprinted with permission from Lee et al. (2015)

1.4 compared to the initial measurement. This implies that both the resin monomer and curing agent were released from the damaged fiber cores; they not only heal the composite, but also strengthen it. The healing PDMS resin is identical to that of the matrix, facilitating compatibility. In contrast, the composite containing PAN NFs shows significant deterioration of its stiffness under repeated tensile testing.

It should be emphasized that the comparison between monolithic PAN and PRC core-shell fiber mats and composites embedded with them is based not on their respective stiffness, but on their respective abilities to recover their original stiffness after repeated moderate stretching or one catastrophic plastic deformation under tension. Therefore, the differences observed between the monolithic PAN NF mats and PRC fiber mats, as well as their respective composites, can be safely attributed

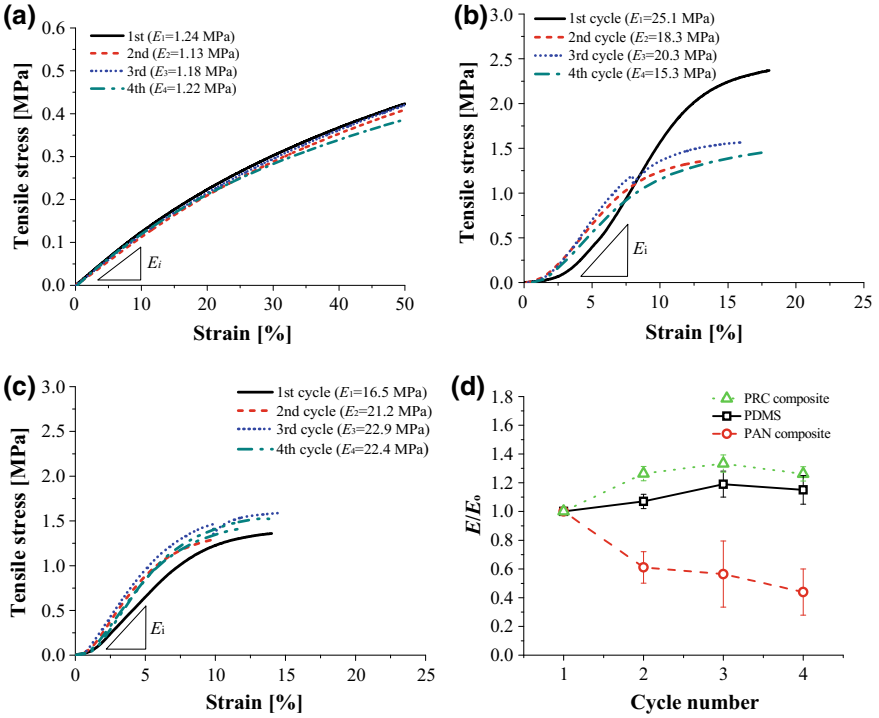

Fig. 7.5 Stress–strain curves of: **a** Pure PDMS, **b** PAN-based composites, **c** PRC self-healing composites, **d** relative Young's moduli; the Young's modulus measured during the first stretching is denoted E_0, while those measured during the sequential tensile tests of the same specimen are denoted E. Reprinted with permission from Lee et al. (2015)

only to the effect of the healing agents released from the damaged cores of the self-healing PRC NFs.

Note also that the restoration of mechanical properties in a 24-h rest period at room temperature, as demonstrated in this section, is an attractive result that fully meets practical requirements. In airplanes, fatigue microcracks accumulate for years, and their partial daily healing could probably prevent such catastrophic events as the opening of a "football-sized" hole in aircraft fuselages, as in 2009 and 2011 during commercial flights (cf. Sect. 1.1). Self-healing caused by different healing agents encased in capsules after the rest periods of 24–48 h at elevated temperatures was reported in Coope et al. (2011, 2014).

7.2 Tensile Testing: Stiffness Recovery in Composites with Solution-Blown PVDF/PEO/Epoxy/Hardener NFs

Solution-blown core-shell NF mats with epoxy resin and hardener (cf. Sect. 2.3) embedded as healing agents in the cores were formed by Lee et al. (2016a) using coaxial solution blowing, as described in Sect. 4.5. The epoxy resin and hardener solidify much faster than the DMS resin monomer and curing agent considered in Sect. 7.1. Therefore, faster self-healing is expected in the present case. The polyvinylidene fluoride/polyethylene oxide (PVDF/PEO) solution, as described in Sect. 4.5, was used to form the NF shells. The solution-blown NF mats with and without epoxy were cut into 20 mm × 60 mm strips. Separately, DMS resin monomer and curing agent were mixed in a 10:1 ratio and the cut fiber strips were cast into the premixed PDMS. The PDMS matrices with the encased fiber strips were allowed to cure in open air at room temperature for 24–48 h. The thickness of each composite specimen prepared according to this procedure was then measured at three different locations, with the average values recorded and listed below. The uniformity of the composites was not fully controlled because the NF mats were not distributed uniformly within the PDMS matrix. The thicknesses of the as-spun NF mat were approximately 0.11–0.12 mm, while the thicknesses of the composite specimens with and without epoxy resin and hardener in the NF cores were approximately 0.53–0.67 mm. An embedded NF mat in a similar PDMS matrix is shown in Fig. 4.30 in Sect. 4.7.

The PDMS–fiber composite specimens were used in tensile tests where the tensile stress was increasing over time in dynamic loading, as in Sect. 7.1. In the present dynamic tensile tests with pre-notched incisions (crack) the upper and lower ends of the composite specimens are tightly gripped by the grips of an Instron machine (model 5942) with a 100-N load cell. The initial gap between the upper and lower grips is 20 mm for all experiments. An initial horizontal incision is pre-notched in the middle of the specimen, as shown in the magnified image in Fig. 7.6. The specimens are then uniaxially stretched at strain rates of either $\dot{\varepsilon}_{xx} = 0.05$ mm/min (= 3 mm/h) or $\dot{\varepsilon}_{xx} = 0.025$ mm/min (= 1.5 mm/h) by the motion of the upper grip. The lower grip remains stationary. This initial stretching is done until the elongation reaches $\ell = 3$ mm in addition to the initial 20-mm gap (for 1 h or 2 h, depending on the stretching rate) or $\ell = 1.5$ mm in addition to the 20-mm initial length (for 0.5 h or 1 h, depending on the stretching rate).

The stretching is then stopped and the specimens are held in a stationary position with fixed grips for 1 or 2 h. Because the epoxy resin embedded in the fibers has a hardening time of approximately 1 h, this waiting time is considered sufficient for crack healing to occur in the specimens containing self-healing NFs.

At the end of the waiting time, the second stage of stretching begins. The specimen stretching is continued at the initial stretching rate until failure occurs by the central crack reaching a catastrophic size. The stress–strain curve for the entire experiment, including both the first and second stages of stretching, is measured by the Instron machine. Simultaneously, a digital camera is used to photograph the specimen with a focus on the propagating crack. Photographs are obtained at regular intervals of

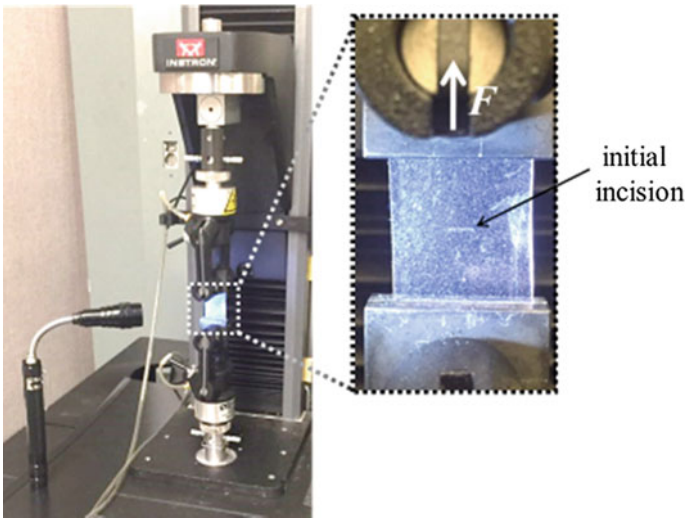

Fig. 7.6 Setup for dynamic tensile tests with crack growth for PDMS–fiber composites at fixed strain rates using Instron machine. The magnified image on the right shows the loaded specimen with the initial pre-notched incision before testing. The healing agents embedded in the fiber cores are the epoxy and hardener. Reprinted with permission from Lee et al. (2016a)

1 min until the specimen fails. All the experiments are repeated at least twice to corroborate the results.

The solution-blown NFs form randomly oriented nonwoven fabrics. The contents of NFs in the PDMS matrices in the composites studied here are approximately 3.21 wt% and 2.68 wt% core-shell NFs with epoxy resin or hardener in the cores and NFs without healing agents, respectively. The Young's moduli of the PVDF/PEO NF mats with and without epoxy and hardener are 2.13 and 2.73 MPa, respectively. Compared to the pure PDMS matrix (E = 0.85 MPa), the PVDF/PEO NF mats are stiffer and stronger by a factor of approximately 2.5–3.2 (see Fig. 7.7). It should be emphasized that the stretching of the NF mats is accompanied by fiber reorientation, predominantly in the stretching direction. Debonding and fiber rupture are minor for the strains of $\varepsilon_{xx} = 7.5$ or 15% explored in the experiments on self-healing depicted in Figs. 7.8 and 7.9, because the slopes of the stress–strain curves remain essentially unchanged.

The stress–strain curves, along with the time-dependent crack lengths, for the specimens containing NFs with and without epoxy components subjected to tensile testing at the constant stretching rate of 3 mm/h are shown in Fig. 7.8. In all cases, (#-1) indicates specimens with only PVDF/PEO fibers (non-self-healing fibers without healing agents), while (#-2) indicates specimens containing self-healing fibers with the epoxy components. Initially, the composite specimens are stretched for 1 h (3 mm, 15% strain) and then held for 1 h before further stretching (Fig. 7.8a-1 and a-2). By the nature of the epoxy, the 1-h holding time should be sufficient for the healing of the

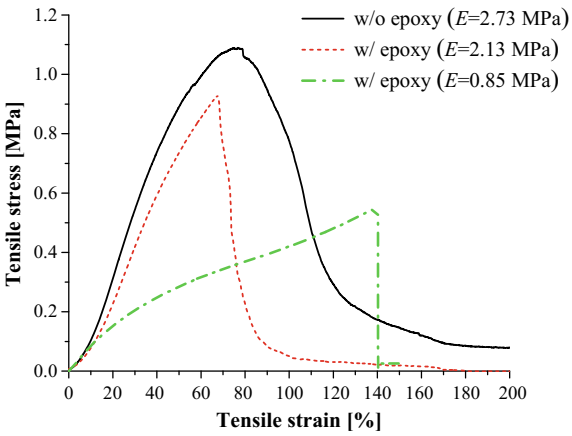

Fig. 7.7 Stress–strain curve of the as-spun PVDF/PEO NF mat with (w/) and without (w/o) epoxy resin and hardener and that of neat PDMS. Reprinted with permission from Lee et al. (2016a)

composite specimens with the epoxy–and hardener-containing NFs. In general, the composites fail at ~25% strain. Hence, 1 h of stretching causing 15% strain should provide moderate damage to the specimens, enough for the composites with the epoxy components to heal, but without causing irreparable damage. Moreover, this moderate damage ensures that only the NFs within the PDMS matrix are ruptured by stretching, while the external PDMS remains intact in the reversible region of elastic deformation. It should be emphasized that the encased NFs are both stiffer and stronger than the PDMS matrix (cf. Fig. 7.7), so the experiments reach the level of fiber damage that could trigger the observations of self-healing effects.

For the next set of tests, the initial stretching time is reduced to 30 min (1.5 mm, 7.5% strain), thereby inflicting less damage to the specimens (Fig. 7.8b-1 and b-2). The holding time remains 1 h.

For the third set of tests, the initial stretching time is 1 h (3 mm, 15% strain), as in the first set. However, the holding time is increased from 1 to 2 h, to elucidate the effects of the holding time on the reaction of the resin and hardener, solidification of the epoxy, and self-healing behavior of the composites.

For the first set of tests, the stress–strain curves for the composites containing PVDF/PEO NFs alone before and after the holding periods show nearly equal slopes, with a decrease of ~0.3% recorded after holding, indicating that no increase in stiffness occurs during the 1-h holding period (Fig. 7.8a-1). Because these NFs contain no self-healing material, the holding period should neither affect the stiffness nor induce healing of the composite. Meanwhile, the composites with NFs containing epoxy components show a remarkable enhancement in stiffness after the holding period (Fig. 7.8a-2). This indicates that the 1-h holding period is sufficient for the reaction between the two components (the epoxy resin and hardener) of the cured epoxy. The Young's moduli for these specimens are dramatically increased by 57.3% from $E_1 = 1.156$ to $E_2 = 1.818$ MPa in the post-holding stretching stage, implying significant self-healing of the composites.

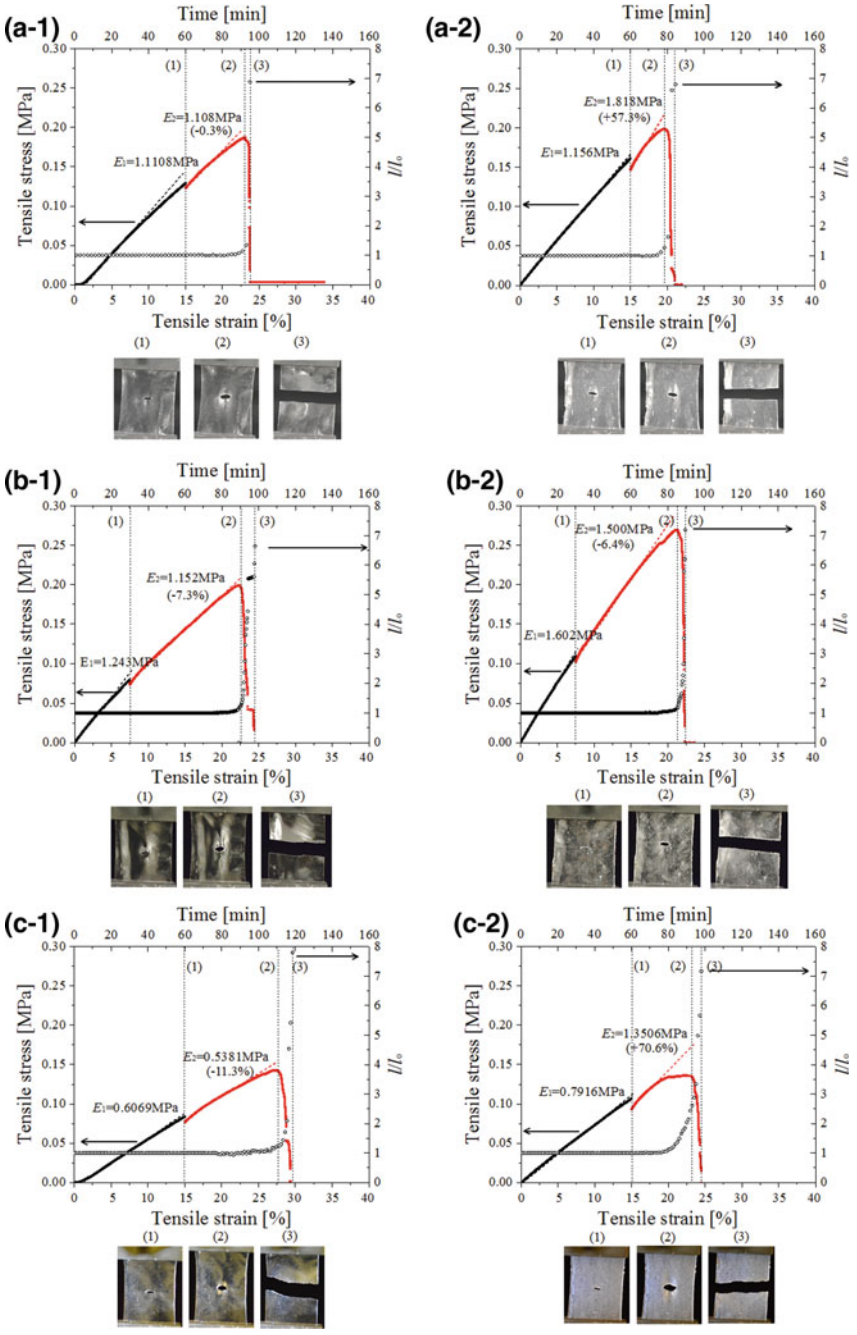
(a-1)
Time [min]
Tensile stress [MPa]
Tensile strain [%]
E₂=1.108MPa
(-0.3%)
E₁=1.1108MPa
(a-2)
E₂=1.818MPa
(+57.3%)
E₁=1.156MPa
(b-1)
E₂=1.152MPa
(-7.3%)
E₁=1.243MPa
(b-2)
E₂=1.500MPa
(-6.4%)
E₁=1.602MPa
(c-1)
E₂=0.5381MPa
(-11.3%)
E₁=0.6069MPa
(c-2)
E₂=1.3506MPa
(+70.6%)
E₁=0.7916MPa

◀**Fig. 7.8** Stress–strain curves and normalized crack lengths (ℓ/ℓ_0) in tensile testing of composites without and with epoxy components encapsulated in embedded NFs at the strain rate of 3 mm/h (= 0.05 mm/min). Panels **a**: stretching length 3 mm, holding period 1 h. Panels **b**: stretching length 1.5 mm, holding period 1 h. Panels **c**: stretching length 3 mm, holding period 2 h. Suffix–1 indicates specimens with PVDF/PEO fibers alone (no healing agents); suffix–2 indicates specimens containing NFs with epoxy components (healing agents) in the cores. In each panel, the black and red bold symbols indicate the initial and post-holding stretching stages, respectively. Black open circles indicate the dimensionless crack length versus time. The photographs of the composite specimens labeled (1), (2), and (3) beneath each stress–strain curve depict the specimens at the end of the holding period, the point of the maximum stress, and after complete failure. Reprinted with permission from Lee et al. (2016a)

For the second set of tests, in which the specimens are initially stretched for less time interval (30 min instead of 1 h), no increase in stiffness is observed, even for the composites containing NFs with the epoxy components (Fig. 7.8b-2). This indicates that the damage caused by 7.5% strain is insufficient to cause NF rupture and the release of the self-healing agents. Therefore, no healing is observed. The stiffness and Young's moduli of these composites, even those containing self-healing NFs are unchanged before and after the holding period.

For the third set of tests, a strain of 15% is applied to the specimens before the holding period. The holding time for these tests was increased to 2 h. As expected, the composites with PVDF/PEO NFs alone reveal no increase in stiffness during the stretching after the holding period (Fig. 7.8c-1). The stiffness is instead decreased by 11.3%. Meanwhile, the composites containing self-healing NFs show a remarkable increase in stiffness when the specimens are stretched after the 2-h holding period, with the Young's moduli increasing by ~ 70.6% from $E_1 = 0.7916$ to $E_2 = 1.3506$ MPa (Fig. 7.8c-2). The opposite trends in stiffness observed for the specimens with NFs with and without the epoxy components demonstrate that the latter specimens are damaged by stretching and inherently deteriorate in their mechanical properties, thereby showing reductions in stiffness. However, the composites with the epoxy components experience self-healing during the healing period of 2 h, causing enhancement of stiffness. The increase in stiffness for the epoxy-containing composites over the 2-h holding time is more pronounced than that observed over the shorter 1-h holding time, indicating that longer holding times permit greater healing in the specimens. Thus, in both cases when the self-healing specimens are moderately damaged, the epoxy cures the damaged sites, thus increasing the composite stiffness.

The crack length measurements over time reveal that the crack length remains nearly constant throughout the tensile tests, except during the final stages when the tensile stress is maximized. This is evident from the normalized crack length ℓ/ℓ_0 (where ℓ_0 is the initial crack length) remaining equal to 1 for most of the tensile test. However, this does not mean that the cracks do not grow and no damage is caused. Subcritical crack growth is possible, but visually difficult to detect [cf. Sect. 6.5 and Lee et al. (2016b), as well as Cherepanov (1979) and Barenblatt (2014)]. As the stress approaches the critical maximum value, the crack begins propagating rapidly, and

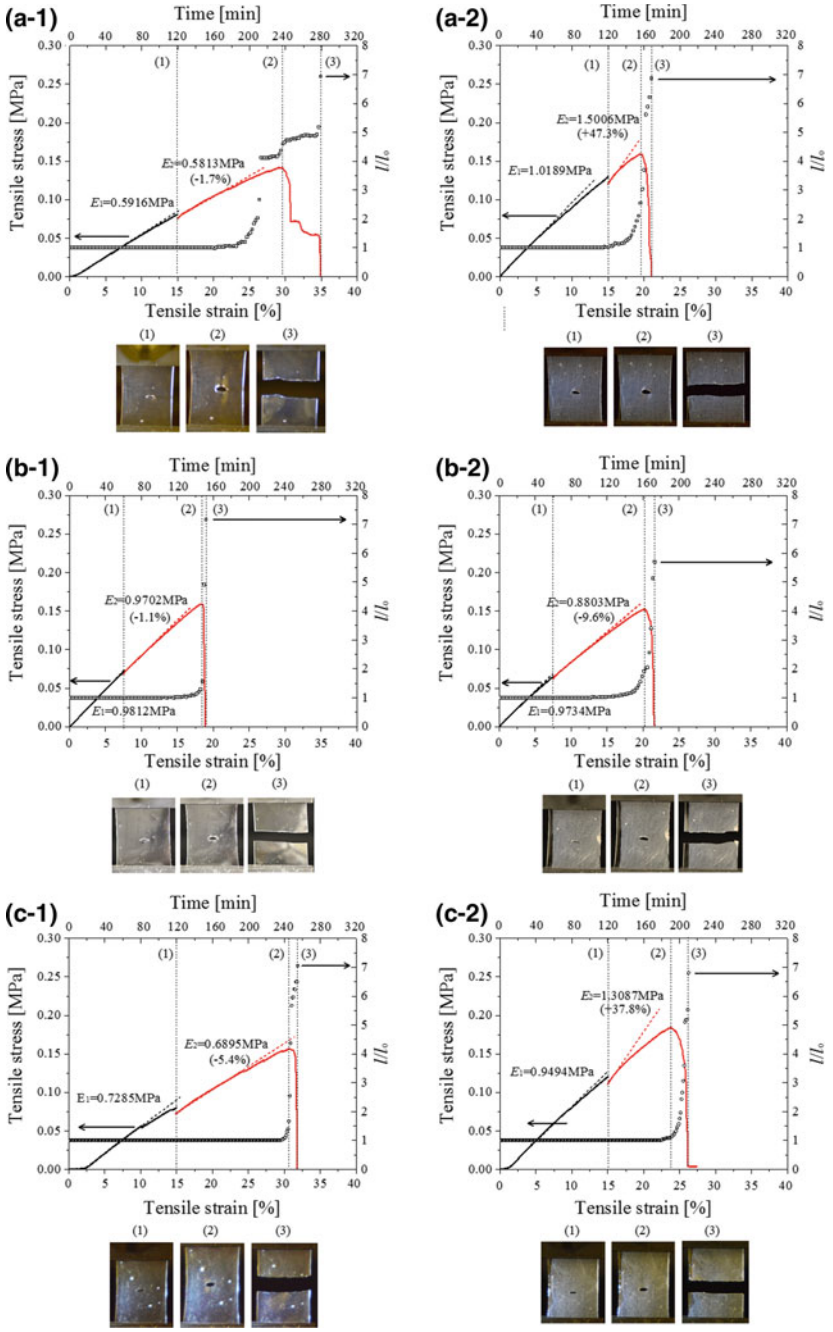
(a-1)
Time [min]
Tensile stress [MPa]
Tensile strain [%]
E1=0.5916MPa
E2=0.5813MPa
(-1.7%)
(a-2)
E1=1.0189MPa
E2=1.5006MPa
(+47.3%)
(b-1)
E1=0.9812MPa
E2=0.9702MPa
(-1.1%)
(b-2)
E1=0.9734MPa
E2=0.8803MPa
(-9.6%)
(c-1)
E1=0.7285MPa
E2=0.6895MPa
(-5.4%)
(c-2)
E1=0.9494MPa
E2=1.3087MPa
(+37.8%)

◀**Fig. 7.9** Stress–strain curves and normalized crack lengths (ℓ/ℓ_0) in tensile tests of composites without and with epoxy components at the strain rate of 1.5 mm/h (= 0.025 mm/min). Panels **a** : stretching length 3 mm, holding period 1 h. Panels **b** : stretching length 1.5 mm, holding period 1 h. Panels **c** : stretching length 3 mm, holding time 2 h. Suffix–1 indicates specimens with PVDF/PEO fibers alone (no healing agents) and suffix–2 indicates specimens containing fibers with epoxy components (the healing agents) in the cores. In each panel, the black and red bold symbols correspond to the initial and post-holding stages of stretching, respectively. The black open circles correspond to the dimensionless crack lengths versus time. The photographs of the composite specimens labeled (1), (2), and (3) underneath the stress–strain curves depict the specimens at the end of the holding period, the point of the maximum stress, and after complete failure. Reprinted with permission from Lee et al. (2016a)

the composite specimen fails within a few minutes. The sudden increase in the crack length is accompanied by the rapid decrease in the tensile stress to zero, indicating the catastrophic failure of the composite specimens.

To study the effect of the stretching rate on the self-healing of the composites, tensile tests are also performed at the lower strain rate of 0.025 mm/min (0.15 mm/h) for different initial stretching times and different holding periods. The results shown in Fig. 7.9, are similar to those in Fig. 7.8. Namely, the composites containing only PVDF/PEO fibers reveal, as expected, no enhancement in stiffness after the holding period (Fig. 7.9a-1, b-1, and c-1) regardless of the holding position or time. A significant increase in stiffness is observed for the composites containing fibers with epoxy components for the initial stretching of 3 mm (2 h of stretching to 15% strain). A holding period of 1 h yields a ~ 47.3% increase in the Young's modulus (Fig. 7.9a-2), whereas a 2-h holding period allows a ~37.8% increase (Fig. 7.9c-2). Unlike the case with the higher strain rate shown in Fig. 7.8, in the present case, the longer holding period does not cause further increases in stiffness. This could be because the lower stretching rate causes less damage to the epoxy-component-containing NFs compared to the previous case shown in Fig. 7.8.

Curing may occur at the initially pre-notched crack, as at any crack, but it elapses over several hours. Therefore, the initial incision may release the epoxy resin and hardener but curing cannot not happen immediately or during the stretching to the strains of $\varepsilon_{xx} = 7.5$ or 15% as shown in positions (1) in Figs. 7.8 and 7.9. During this first stage of stretching, the slopes of the stress–strain curves are not visibly changed, corroborating the lack of curing during these relatively short periods of time, despite the epoxy resin and hardener released from the initial and growing cracks. Afterward, a rest (holding) period of t = 1–2 h is given, which is sufficient for the curing reaction to proceed. Accordingly, in the second stretching stage after the holding period, an increase in stiffness is observed, which is caused by self-healing, i.e., curing and hardening of the released epoxy resin.

The microscopic phenomena accompanying self-healing are revealed in Fig. 7.10, showing SEM images of the specimen surface fractured by crack propagation. In the left-hand panel in Fig. 7.10, the fractured PDMS surface resembles a brick wall near the panel bottom. However, in the middle of the magnified specimen in the

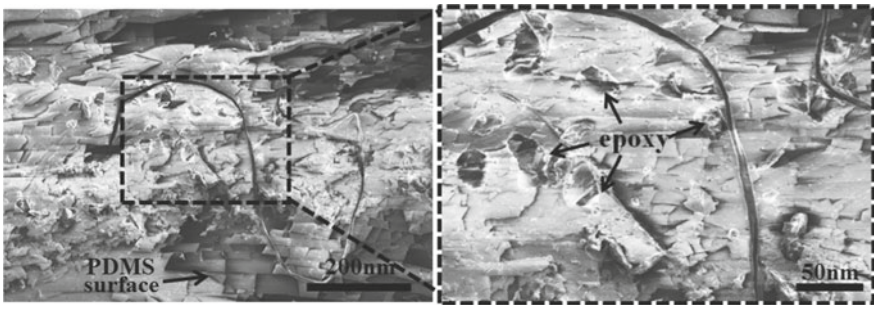

Fig. 7.10 SEM micrographs of fractured surface of a composite specimen containing self-healing NFs. Reprinted with permission from Lee et al. (2016a)

right-hand panel, several irregular epoxy chunks released from the fractured NFs are clearly visible.

Overall, the self-healing composites show the ability to restore and even enhance their mechanical stiffness after sustaining moderate damage, with healing times on the scale of 1 day for the DMS resin/curing agent (cf. Sect. 7.1) and 1 h for the epoxy/hardener healing agents, as shown in the present section. Repeatable self-healing is possible. However, self-healing is impossible after near-catastrophic damage.

7.3 Strength Recovery Under Static Fatigue Conditions

Considering the self-healing of fatigue cracks in self-healing composites, Lee et al. (2016b) studied composite materials with embedded epoxy/hardener-containing core-shell nanofibers formed by solution blowing (cf. Sect. 4.5). The shells of the core-shell solution-blown fibers were formed from a PVDF/PEO mixture. The core-shell fibers were encased in a PDMS matrix (see Fig. 4.30 in Sect. 4.7). An initial incision in the middle of a composite specimen stretched in a static fatigue test can, in principle, experience either crack propagation or healing, as observed in the present experiments.

The self-healing composite specimens are gripped between two vertical bars. The upper grip is fixed, while the lower one moves in the vertical direction (Fig. 7.11). Initially, a 20-mm-long specimen is clamped between the two grips (Fig. 7.12a). A 4-mm-long ($\ell_0 = 4$ mm) horizontal incision is introduced to the middle of the specimen. By lowering the lower grip mechanically, the specimens are stretched by 3, 3.5, or 4 mm, corresponding to 15%, 17.5%, or 20% of the initial length, respectively (Fig. 7.12b). A vertical micrometer fixed behind the grips facilitates the accurate measurements of the stretched specimen lengths. The horizontal incision in the original specimen is oval in shape. This is attributed to the initial stretching (cf. Fig. 7.12a and b). After the initial stretching, the upper and lower grips are fixed,

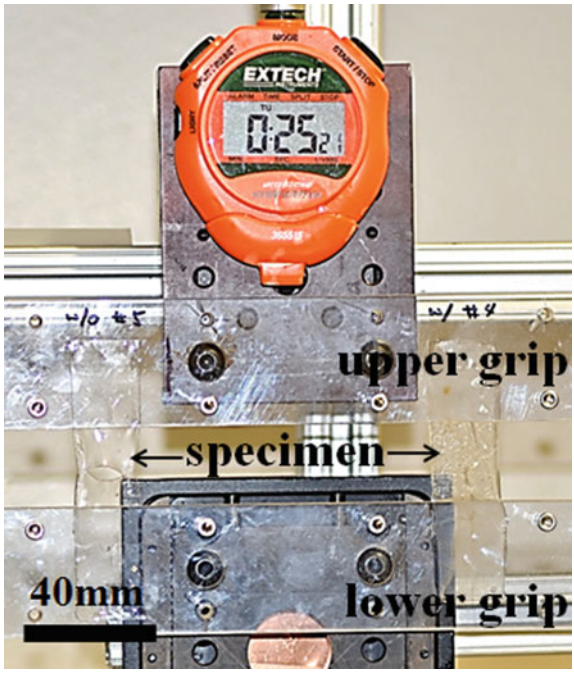

Fig. 7.11 Fatigue test setup with the fixed upper grip and movable lower grip. Reprinted with permission from Lee et al. (2016b)

thereby fixing the stretched specimen length in the vertical direction for a long time, during which the incision in the middle of the specimen is permitted to evolve. Hence, the stretching strain applied to the specimen in the vertical direction remaines fixed throughout the experiment. Snapshots of the specimen are taken every 30 min to monitor the increase in the crack length, ℓ, with time. It should be emphasized that the specimens are subjected to moderate tensile stresses and that the evolution of the fatigue crack in the self-healing or control specimens took hours or days, sufficient for self-healing.

Figure 7.13 shows the as-spun solution-blown fibers without epoxy before they are embedded in the PDMS matrix. The average diameter of fibers without and with epoxy components are 620 and 980 nm, respectively. Detailed descriptions of the fibers, their morphologies and diameter distributions are available in Sect. 4.5. The crack length ℓ is measured as a function of time using the photographs of the specimens obtained at various time moments t during the fatigue process. At $t = 0$, the dimensional length $\ell_0 = 4$ mm, and the dimensionless ratio $\ell/\ell_0 = 1$.

To explore the effects of the embedded NFs on the mechanical properties of the PDMS matrices, tensile tests of the different specimens were performed using an Instron 5942 with a 100-N load cell. The Young's modulus was measured using 20 mm × 60 mm specimens at a fixed strain rate of 10 mm/min. The Young's moduli of pure PDMS, self-healing PVDF/PEO NF mats, and non-self-healing mats were 1.24, 2.13 and 2.73 MPa, respectively. The Young's moduli of the PDMS–PVDF/PEO

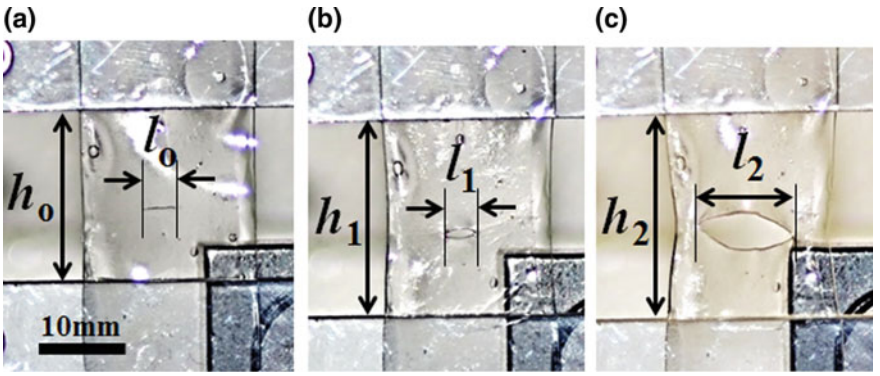

Fig. 7.12 Fatigue tests of PDMS–PVDF/PEO composites with and without epoxy and hardener in the cores of the embedded fibers. **a** The 20-mm-long specimens ($h_0 = 20$ mm) are initially clamped between the upper and lower grips, and **b** stretched by 3–4 mm ($h_1 = 23$–24 mm). **c** An increase in the crack length in time is revealed by a photograph taken at t = 6 days. Reprinted with permission from Lee et al. (2016b)

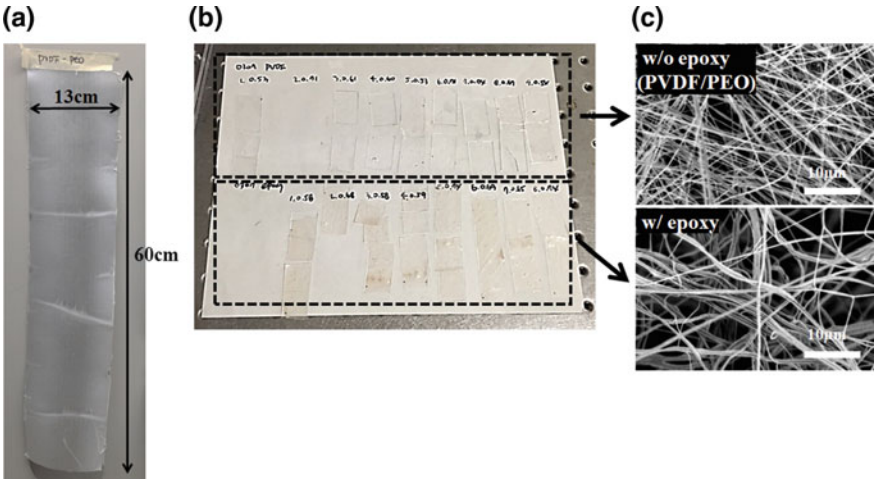

Fig. 7.13 **a** Solution-blown fiber mat collected on the plastic mesh of a rotating drum. **b** Specimens with the fiber mats encased in PDMS matrices. **c** SEM images of fibers with and without epoxy resin or hardener. Reprinted with permission from Lee et al. (2016b)

composites with and without epoxy and hardener in the NF cores were 1.53 and 1.44 MPa, respectively. Therefore, in this case the stiffness of the PDMS matrix was increased (not decreased) by 16–23% after the NFs were embedded.

In the experiments with the stretched composite specimens with cracks, distinctly different behaviors are recorded for the two types of specimens, i.e., for those with and without epoxy resin or hardener. For the composite specimens containing the PVDF/PEO fibers without epoxy resin or hardener, the crack length increases signif-

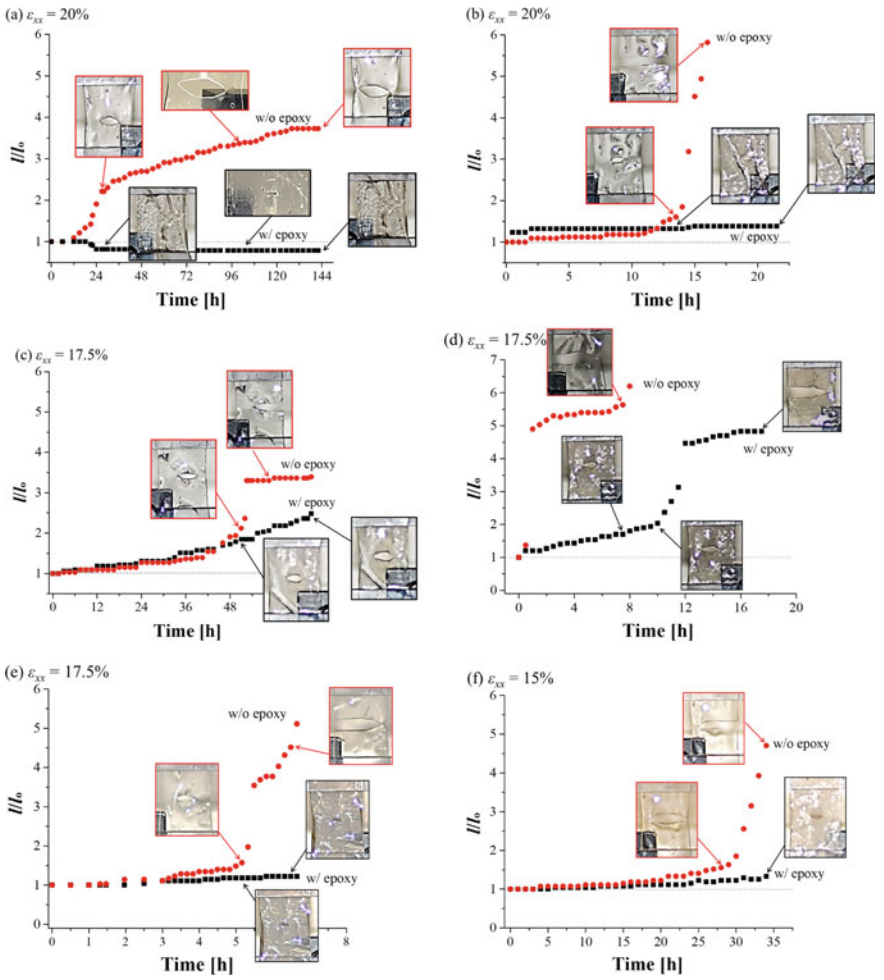

Fig. 7.14 Static fatigue test under fixed strain. The data for the composite specimens comprising PDMS matrices with embedded fibers without epoxy resin and hardener and those with epoxy resin and hardener are shown in red dots and black squares, respectively. The specimen thicknesses without and with epoxy are, respectively, **a** 0.44 and 0.63 mm, **b** 0.64 and 0.63 mm, **c** 0.77 and 0.49 mm, **d** 0.70 and 0.48 mm, **e** 0.60 mm for both, and **f** 0.53 and 0.58 mm. The strains ε_{xx} applied to the specimens are: **a**–**b** $\varepsilon_{xx} = 20\%$, **c**–**e** $\varepsilon_{xx} = 17.5\%$, and **f** $\varepsilon_{xx} = 15.0\%$. The thicknesses of the solution-blown fiber mats, both without and with epoxy components, before being encased in the PDMS matrix were in the 0.03–0.04 mm range. Reprinted with permission from Lee et al. (2016b)

icantly after the first 24 h and continues to increase until specimen rupture. However, for the specimens containing the fibers with epoxy resin and hardener, the crack propagation is much slower, indicating self-healing in the specimens. In fact, as Fig. 7.14a shows, the crack length in the self-healing specimens even decreases with time.

It should be emphasized that the composite specimens with the same contents, almost the same initial strains, and almost the same thickness can show different behaviors. These differences are attributed to several factors. First, the distribution of the fiber mat in the PDMS matrix cannot be precisely controlled; hence, after the setting, the fiber distribution is not uniform inside the PDMS matrix. Crack propagation is monitored in the center of the composite specimen, and the fiber content around the initial incision is uncontrollable for specimens both with and without epoxy. For the epoxy-containing specimens, the distribution of the epoxy within the encapsulated fiber is also unknown, because the core-shell fibers themselves are not uniform and the mat thickness near the initial incision may vary. Second, PDMS requires ~24–48 h to cure; although the initial thicknesses of the fiber mat-containing specimens are equal, the final thicknesses of the composites differ significantly. Accordingly, the time of specimen failure varies from 7 h to 6 days for the abovementioned reasons.

Under a fixed tensile strain, the crack length remains similar to the initial crack length ℓ_0 for some time. However, the crack length eventually begins to visibly increase. The increase in the crack length is much slower for the specimens containing fibers with the epoxy components, as the static fatigue tests are sufficiently long to allow the epoxy resin and hardener to escape the ruptured fibers, conglutinate, and solidify, and thus heal the specimen. The epoxy resin and hardener released from the separate broken fibers are cured along the crack and at the crack tip, which significantly delayed the crack propagation, as indicated by Fig. 7.14. The figure shows that the dimensionless crack lengths for the specimens with the embedded epoxy-component-containing fibers remain constant near 1 for most cases. Because the static fatigue tests last for several hours or days, while the epoxy requires only 1 h to cure, they facilitate the crack arrest in the self-healing specimens. It is also interesting to note that the subcritical cracks grow in a stepwise manner before reaching critical sizes, after which they grow continuously until they destroy the specimen. This trend is visible in both types of specimens, i.e., those with and without the epoxy resin and hardener. The stepwise growth of the subcritical fatigue cracks observed here is explained theoretically in Sect. 6.5.

The result shown in Fig. 7.14e is noteworthy. Here, the initial thicknesses of the composite specimens with and without epoxy are identical at 0.60 mm. Such specimens can be compared directly by ruling out the possible influence of the specimen thickness on the fatigue process. The self-healing epoxy-component-containing specimen still outlives that without epoxy, as shown in Fig. 7.14e, thus demonstrating the self-healing phenomenon. In addition, for the cases shown in Fig. 7.14c and d, the epoxy-component-containing self-healing specimens are thinner than those without epoxy. Regardless, the former outlive the latter because of the self-healing process.

7.4 Dynamic Situation: Mode I Crack Propagation

Co-electrospun PRC, PAN–resin (PR) and PAN–curing agent (PC) NF mats described in Sect. 4.2, and control electrospun pristine PAN mats were analyzed in tensile tests with progressively increasing stress to observe the influence of healing agents on the evolution and propagation of cracks pre-notched on one side in the middle of the mats (Lee et al. 2017). The Instron 5942 machine was used to conduct the tests. The tensile tests of the NF mats and the fiber-reinforced composite specimens were conducted according to ASTM D7565 standard (Standard 2017). The specimens were prepared by cutting the NF mats along the machine direction into rectangular strips of 60 mm × 25 mm (length × width) in size. These rectangular mats were then fixed in the Instron 5942 machine by clamping the upper and lower ends of the mats with pneumatic grips, with the two clamps separated by 20 mm. Thus, each exposed specimen had an initial area of 20 mm × 25 mm. A 5-mm-long sharp crack was pre-notched in the middle of each mat on the right-hand side, as shown in Fig. 7.15b. Then, the specimens are stretched at strain rates of 50, 10 and 1 mm/min until complete failure due to crack propagation (Mode I fracture; cf. Sect. 6.2). The load–displacement data obtained from the tensile tests were converted into the corresponding stress–strain curves; video imaging of crack propagation through the mats was conducted simultaneously. It should be emphasized that the cross-sectional area was evaluated as the product of the thickness and width of the mat, thus neglecting the cross-sectional porosity. Stretching is known to diminish the cross-sectional porosity of NF mats. Accordingly, the introduced inaccuracy is decreased as the stress and strain increase.

Representative stress–strain curves for the PAN and PRC specimens measured in tensile testing with Mode I crack propagation are shown in Fig. 7.16a. The corresponding stiffness associated with the initial linear segments of the curves and the ultimate strengths achieved are similar for the PAN and PRC NF mats in the present case. Significant differences between the two curves are observed beyond the ultimate strength point. The strain-at-failure of the PRC specimen is much larger than that of the PAN mat. The PAN mat experiences sudden failure immediately after the maximum stress point; the time interval before its complete failure ($t_{c,\,PAN}$) is short compared to that of the PRC specimen ($t_{c,\,PRC}$). The PRC NF mat cracks gradually for a much longer time. The crack propagation length before complete mat failure is 20 mm, i.e., equal to the difference between the mat width of 25 mm and the initial pre-notched crack length of 5 mm. This propagation length of 20 mm is divided by each crack propagation time (either $t_{c,\,PAN}$ or $t_{c,\,PRC}$) to evaluate the crack propagation speed V.

Several representative images of the PAN and PRC NF mats showing crack propagation during the tensile tests are depicted in Fig. 7.16b and c. The lower grip of the Instron 5942 machine remains fixed throughout the experiment, while the upper grip moves upward at a constant stretching rate. Figure 7.16b and c reveal that only the crack width increases initially, while the crack length remains constant at the pre-notched value of 5 mm. Once the tensile stress reaches its maximum value, indi-

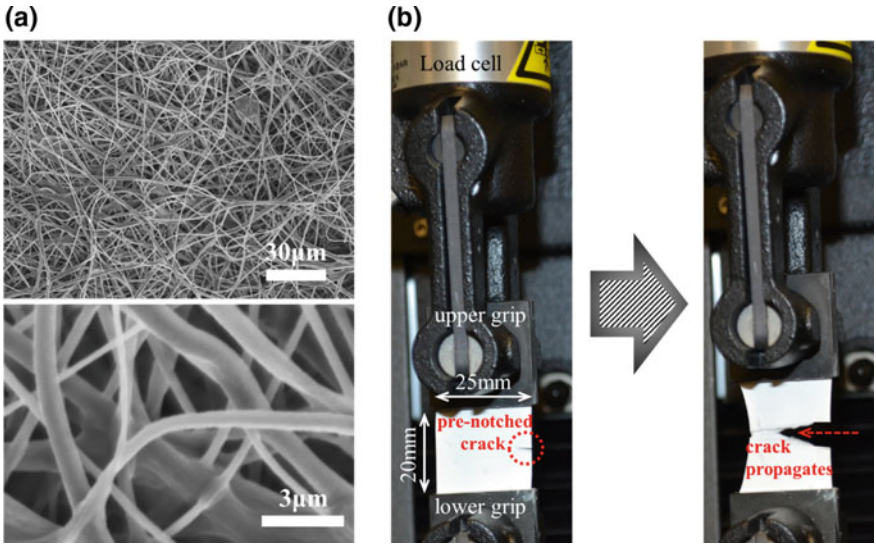

Fig. 7.15 **a** SEM micrographs of as-spun NF mat before damage. **b** The original specimen (as-spun NF mat) held between the grips of the Instron 5942 machine and propagation of the pre-notched crack during the tensile test. Reprinted with permission from Lee et al. (2017)

cating that the mat has reached its ultimate strength the crack propagates horizontally and its length begins to increase. From the images of the mat taken at regular time intervals, the crack propagation rate is measured after the ultimate strength point until the crack reaches the other edge of the mat (cf. the rightmost images in Fig. 7.16b and c).

The tensile tests of the PAN and PRC specimens are repeated at least four times (marked 1–4 in panels in Fig. 7.17a and b) for each stretching rate; thus the averaged Young's moduli and crack propagation speeds are established. Figures 7.17, 7.18, 7.19 summarize the results of the tensile tests conducted at the strain rates of 50, 10 and 1 mm/min, respectively. The catastrophic failure of the PAN NF mats occurs immediately after the maximum strength point, while that of the PRC specimens is delayed to a much larger strain, similar to the data in Fig. 7.16. The crack propagation speed of the PRC specimens is approximately 11% of that of the PAN specimens. In other words, the PRC specimens show much slower crack propagation during the tensile tests, while the Young's moduli of the PAN specimens are approximately 22% higher than those of the PRC specimens. The crack propagation is slowed by the presence of the uncured liquid agents in the cores of the core-shell PRC NF mats because the viscous liquids in the fiber cores provide another channel for energy dissipation. The specific value of the energy dissipation rate is on the order of $\mu(V/d)^2$, with μ being the zero-shear viscosity, V the crack propagation velocity, and d the cross-sectional fiber diameter. The viscous dissipation rate increases dramatically for sufficiently high liquid viscosities and small fiber diameters, as is the case here.

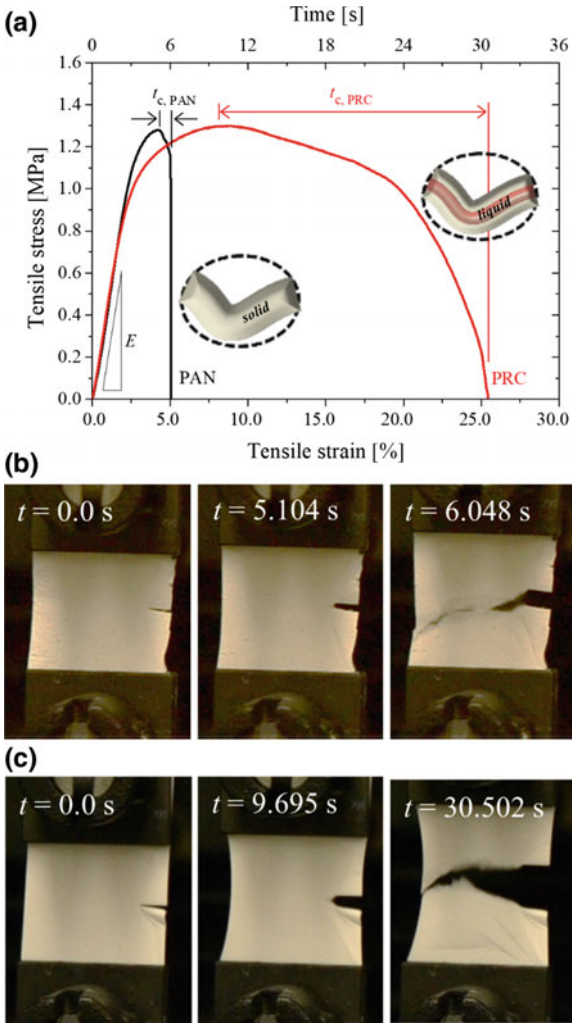

Fig. 7.16 **a** Stress–strain curves measured in tensile tests with pre-notched crack propagation in Mode I. Photographs of **b** PAN and **c** PRC specimens during the tensile tests reveal crack propagation in the horizontal direction beyond the ultimate strength point. The strain rate for the tensile tests is 10 mm/min for both cases. Reprinted with permission from Lee et al. (2017)

This is substantiated by the different rupture times of the PRC and PAN specimens, as Fig. 7.16a shows, of approximately 26 and 5 s, respectively, despite all conditions (fiber diameter, mat thickness, and strain rate) being equal. This indicates the retarding action of the liquid cores, although a detailed micro-mechanical theory for this phenomenon is currently unavailable.

The Young's modulus of the PRC specimens is gradually decreased as the strain rate increases from 1 to 50 mm/min (Fig. 7.20a). Slower stretching corresponds to higher measured stiffness in the PRC specimens, whereas the stiffness of the PAN specimens was approximately constant (cf. Fig. 7.20a). At the lowest stretching rate of 1 mm/min, the Young's moduli of the PAN and PRC specimens are similar. There-

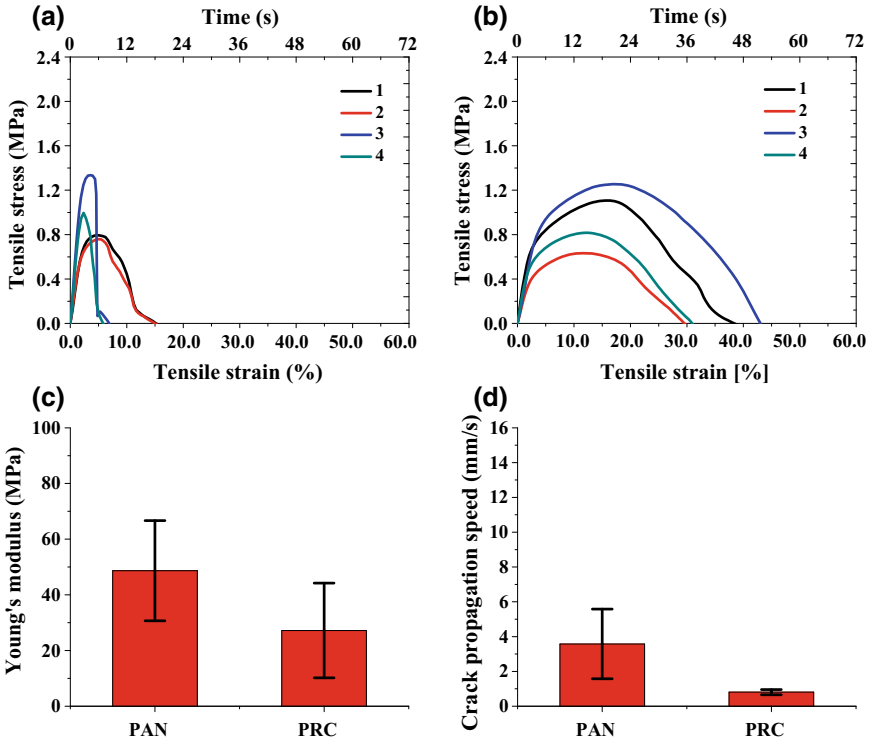

Fig. 7.17 Stress–strain curves of **a** PAN and **b** PRC NF mats in tensile tests with crack propagation. The numerals 1–4 in panels **a** and **b** indicate the four different trials. Averaged **c** Young's moduli and **d** crack propagation speeds for the PAN and PRC mats. Stretching rate is 50 mm/min. Here and hereinafter in Figs. 7.18 and 7.19, four different trials are used to evaluate repeatability. Reprinted with permission from Lee et al. (2017)

after, the Young's modulus is unchanged for the PAN mats, whereas it is decreased for the PRC specimens. The crack propagation speed of the PRC mats is approximately independent of the stretching rate and much lower than that of the PAN mats, which also show stretching rate dependence (Fig. 7.20b). At the lowest stretching rate of 1 mm/min, the crack propagation speeds for the PRC and PAN mats are similar. Thereafter on increasing the stretching rate, the crack propagation speed for the PAN mats is increased significantly, while that of PRC specimens is unchanged. Accordingly, the crack propagation speed at the strain rate of 10 mm/min is approximately 10 times lower for the PRC specimens than that of the PAN specimens.

The strains at which the ultimate stress is attained, denoted the ultimate strain, for the different PAN and PRC mats at different stretching rates are depicted in Fig. 7.20c. Because crack propagation begins only after the ultimate stress, higher ultimate strains imply longer elapsed times before the beginning of crack propagation. This time is denoted by t* in Fig. 7.20c. As seen in this figure, PRC specimens at all

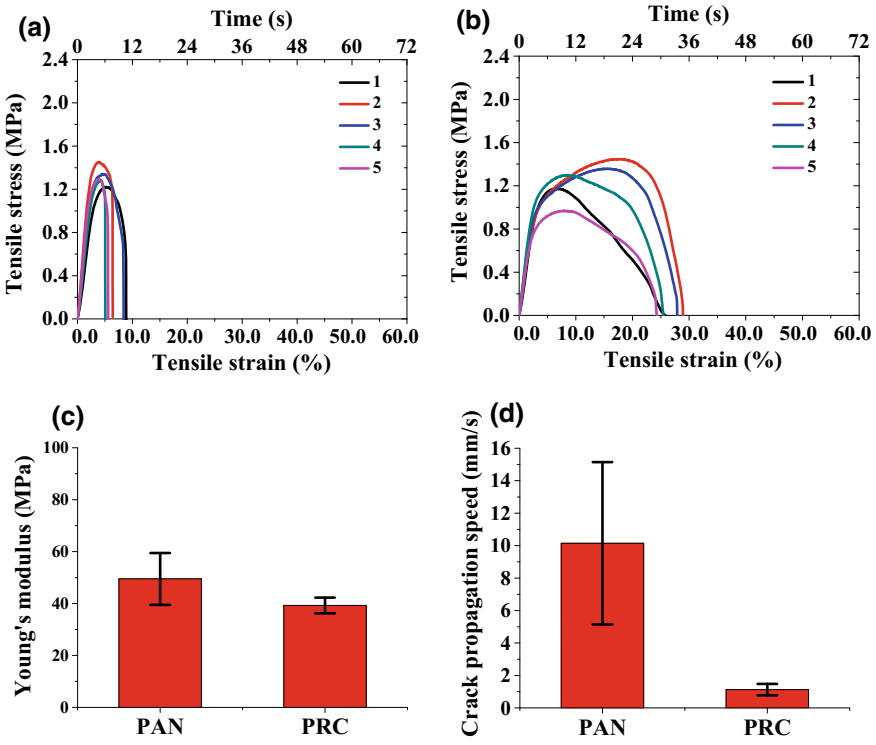

Fig. 7.18 Stress–strain curves of **a** PAN and **b** PRC NF mats in tensile tests with crack propagation. The numerals 1–4 in panels **a** and **b** indicate the four different trials. Averaged **c** Young's moduli and **d** crack propagation speeds for the PAN and PRC mats. Stretching rate is 10 mm/min. Reprinted with permission from Lee et al. (2017)

stretching rates show ultimate stresses at higher strain values than the corresponding PAN specimens. Thus, it can be concluded that the beginning of crack propagation in PRC specimens is delayed as compared to that in PAN specimens.

It should be emphasized that t* is the time interval from the beginning of the tensile tests until the ultimate stress point is reached, whereas t_c is the time interval from the ultimate stress point until a complete mat rupture. Thus, t* indicates the initial delay in crack propagation, while t_c indicates the crack propagation speed in the specimen. Figure 7.20 shows that both t* and t_c are longer for the PRC mats. Hence, it can be concluded that the cracks begin to grow later and more slowly in the PRC mats than those in their counterpart PAN mats.

In comparing the PR and PC fiber mats, their behaviors are quite similar. It should be emphasized that their Young's moduli, the ultimate stresses, and ultimate strains are slightly different from those of the PRC fiber mats. In Fig. 7.20a, the Young's moduli of the PR and PC fiber mats are higher than that of the PRC fiber mat, and even higher than that of the PAN mat at some points. The ultimate stresses and strains

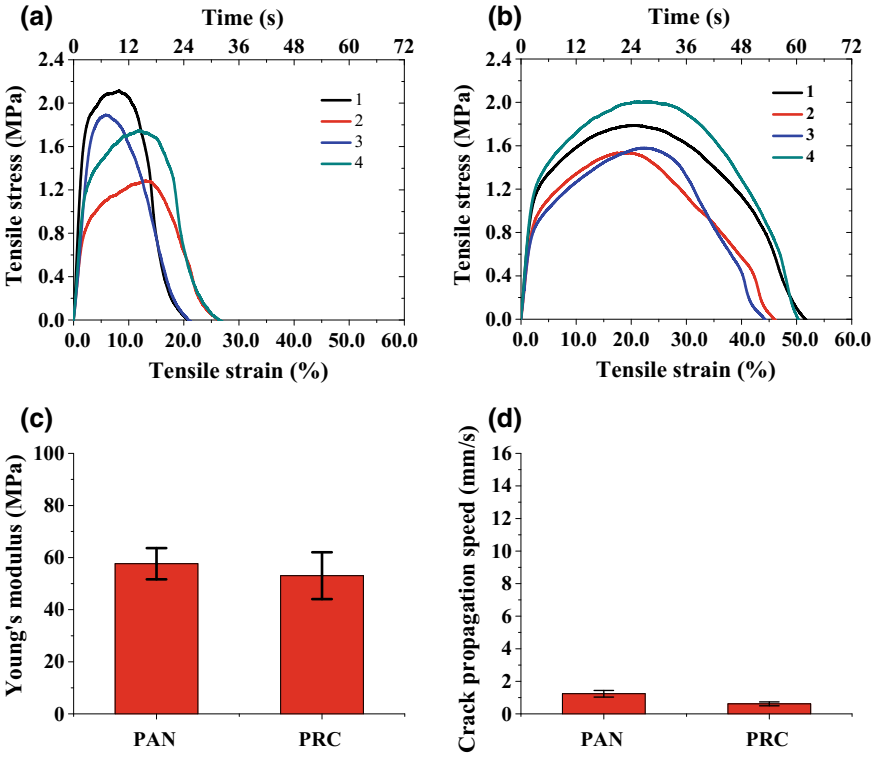

Fig. 7.19 Stress–strain curves of **a** PAN and **b** PRC NF mats in tensile tests with crack propagation. The numerals 1–4 in panels **a** and **b** indicate the four different trials. Averaged **c** Young's moduli and **d** crack propagation speeds for the PAN and PRC mats. Stretching rate is 1 mm/min. Reprinted with permission from Lee et al. (2017)

of the PR and PC fiber mats are higher and lower, respectively, than that of the PRC specimen (see Fig. 7.20c). However, the crack propagation speeds in the PR and PC specimens are similar to that in the PRC specimen, while being lower than that in the PAN specimen for all three strain rates.

Despite the data scatter involved, as manifested by the error bars, Fig. 7.20c reveals a clear delineation of the data for the PRC fiber mats from that for the PAN, PR, and PC fiber mats. Resin polymerization by the curing agents, associated with microscopic damage prior to crack propagation, is present only in the PRC fiber mats among all tested mats, and thus causes the recorded delays in PRC mat failure.

In general, higher applied loads correspond to shorter time intervals t* before the beginning of rupture (Parton and Morozov 1989). The longer time to failure of the PRC specimens as compared to that of the PAN specimens allows speculation that stress relaxation (viscoelastic memory effects) may occur in the PRC specimens. The stress relaxation in the PRC NFs is presumably associated with the presence of the liquid cores in these NFs. In addition to the elastic material parameter of the Young's modulus E associated with the solid polymeric shells of the fibers, another parameter of the zero-shear viscosity μ is associated with

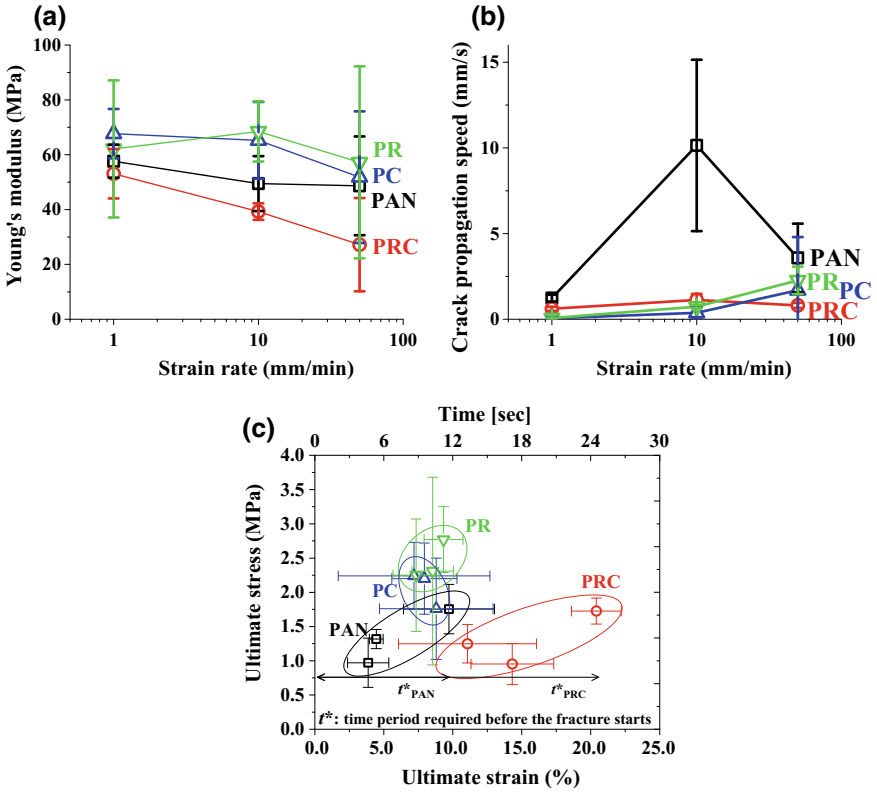

Fig. 7.20 Material parameters of the PAN, PRC, PC and PR mats. **a** Young's moduli. **b** Crack propagation speeds. **c** Ultimate stresses versus ultimate strains. Reprinted with permission from Lee et al. (2017)

the liquid cores. Accordingly, the characteristic stress relaxation time $\theta = \mu/E$ arises, which determines stress relaxation over time t, typically in the form of the exponential fading memory $\exp(-t/\theta)$ (Feng et al. 2002). In addition, liquid in the NF core may act as a plasticizer. Plasticizers are often added during manufacturing to improve the mechanical properties of polymers, facilitating chain rotation and motion with enhanced free volumes between the chains (Lim and Hoag 2013). Plasticizers decrease the Young's modulus and increase stretchability and resistance to cracking (Heinamaki et al. 1994; Leblanc et al. 2007; Joffe et al. 2015). In summary, the presence of liquid epoxy in the fiber cores of the PRC mats may provide an additional energy dissipation channel, granting viscoelasticity and stretchability as well as providing the ability to heal microscopic damage by means of the resin polymerization before and during crack propagation.

The as-spun PRC and PAN NF mats show irregular crack shapes and intermittent crack propagation, as in Fig. 7.16. Therefore, to study the crack shapes and propagation rates, composite specimens were formed with the co-electrospun PRC and electrospun PAN NFs embedded in them. The PAN/PRC NF mat was cut into pieces of 25 mm × 60 mm and then encased in a PDMS (10:1 wt. ratio) matrix. The thicknesses of such the PRC- and PAN-containing composites were 0.61 ± 0.16 mm and 0.52 ± 0.26 mm, respectively. Similarly to the tensile tests of the PRC and PAN NF mats, 5-mm-long sharp cracks were pre-notched in the middle of the right-hand sides of the composite specimens. Then, crack propagation under tension was observed. Similar observations were done using pure PDMS specimens (without the embedded NFs); however, the specimen stiffness in this case did not allow uniform crack propagation, as shown in Fig. 7.21a.

Figure 7.21b and c show the shapes of the cracks as they propagate across the PDMS–PRC and PDMS–PAN composite specimens, respectively. The theoretically predicted shape, assuming Kelvin–Voigt viscoelastic resistance near the tip of the opening crack, is sketched in Fig. 6.4 in Sect. 6.3. Such shapes can, to some extent, resemble the experimental images in Fig. 7.21b–i for various crack lengths and pre-notch positions. The PDMS–PRC and PDMS–PAN specimens with pre-notches at the right sides are shown in panels Fig. 7.21b–c, d, g and e, h with different initial incision lengths of 5, 2 and 10 mm, respectively. The initial incisions are located in the specimen centers in panels Fig. 7.21f and i for the PDMS–PAN and PDMS–PRC specimens, respectively. Overall, the PDMS–PAN and PDMS–PRC specimens show similar trends in crack propagation, smoothness, and uniformity in the crack boundaries and propagation rate. Especially, in Fig. 7.21d, the experimentally observed evolution of the crack shape at the final stages matches well with the theoretical predictions.

The PDMS–PAN composite specimens with the embedded rectangular strips of PAN NF mats have the width $2h = 25$ mm. An initial incision of the length of 5 mm is made at the specimen center (cf. Fig. 7.21f). The initial crack length is, accordingly, $2\ell_0$. The composite PDMS–PAN specimens are then stretched at a uniform stretching rate using an Instron 5942, while photographing the developing crack at regular time intervals. The dimensionless load $\overline{\sigma_\infty}$ is obtained from the stress–strain data, while the dimensionless crack length $\overline{\ell}$ is measured from the snapshots; the definitions of the dimensionless parameters are given in Eq. (6.37) in Sect. 6.4.

Figure 7.22 depicts the results of two experimental trials and compares them with the theoretical lines I and II. Because the parameters K_{Ic} and λ [cf. Eq. (6.37) in Sect. 6.4] are calculated using the values of the maximum stresses and yield stresses, the theoretical curves for each experimental set in Fig. 7.22a and b differ. Initially, the crack growth occurs in the stable subcritical domain, as is seen with the overlap of the experimental data with curves I. As the dimensionless load $\overline{\sigma_\infty}$ continues increasing, the crack length $\overline{\ell}$ crosses from the subcritical to the unstable supercritical and catastrophic domain (crossing curves II). The crack length then begins to increase in an unstable non-monotonic manner, similar to the ideal brittle crack trend (depicted by curves III). This continues beyond the ultimate stress point of the composite until complete specimen rupture.

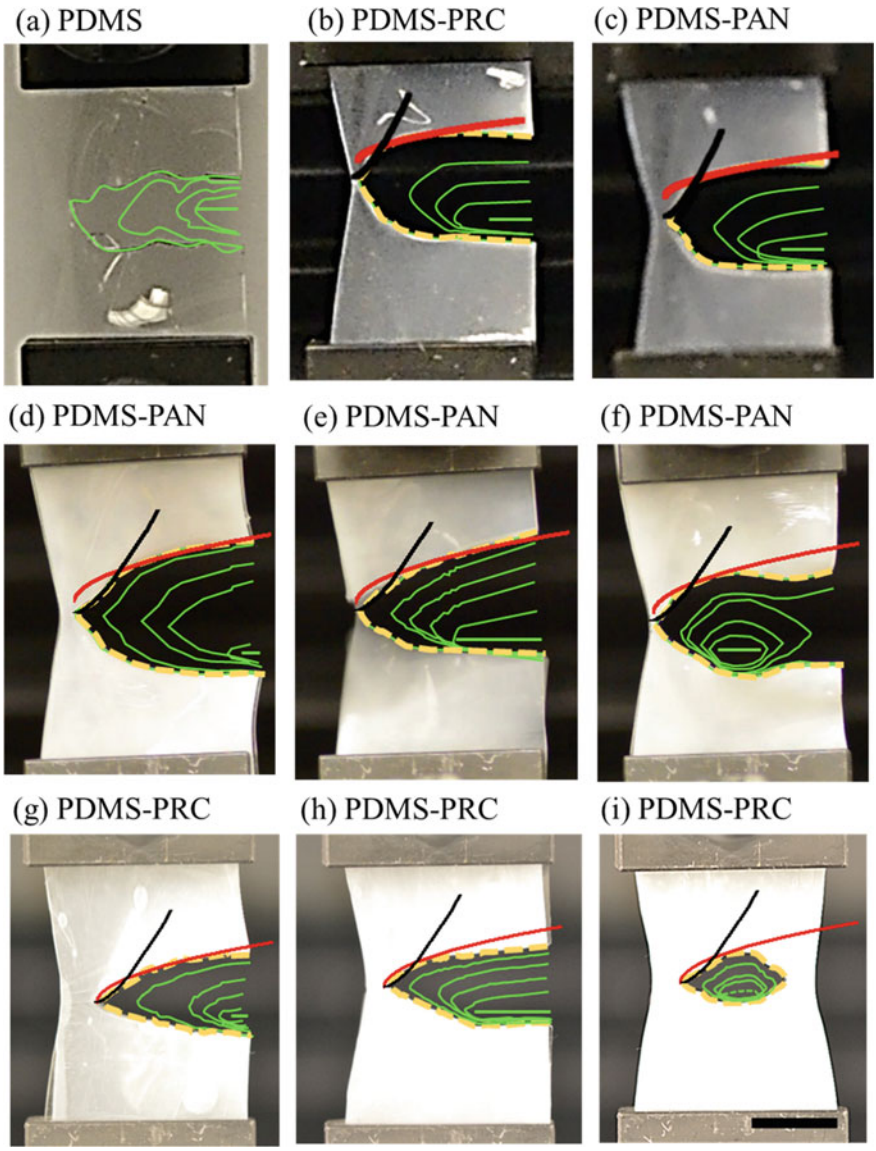

Fig. 7.21 Crack evolution in **a** pure PDMS, **b**, **g**–**i** PDMS–PRC, and **c**–**f** PDMS–PAN composite specimens. The lengths of the pre-notched incisions (shown by solid green horizontal bars): for **a**–**c**, **f**, and **i** $\ell_0 = 5$ mm; for **d**, **g** $\ell_0 = 2$ mm, and for **e**, **h** $\ell_0 = 10$ mm. Initial incision location is on the right side in panels (**a**–**e**, **g**–**h**), and at the center in panels (**f**, **i**). Four different colors are used to demarcate curves with different physical meanings: black is used for the near-field asymptotic, red for the far-field asymptotic, green for the intermediate contours of the propagating cracks, and dashed yellow lines for the final crack shapes. The theoretical predictions, shown by the black and red solid lines, correspond to the asymptotic expressions $[x - \ell(t)]^{3/2}$ and $[x - \ell(t)]^{1/2}$, respectively (cf. Sect. 6.3). The theoretical predictions are compared to the last photographs in all the panels, because the crack appears with the best resolution in these. Scale bar is 10 mm. Reprinted with permission from Lee et al. (2017)

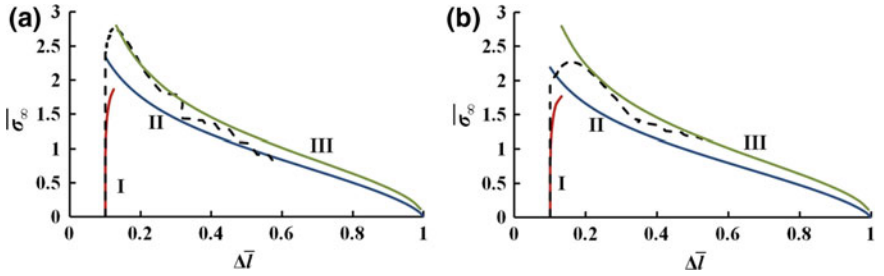

Fig. 7.22 Comparison of the experimental results on crack propagation with the theory of Sect. 6.4 developed for fatigue cracks propagating under load. Panels **a** and **b** indicate two different trials. Red lines I correspond to Eq. (6.39), blue lines II correspond to Eq. (6.38), and green lines III correspond to Eq. (6.40) from Sect. 6.4. The black dashed lines show experimental data. Reprinted with permission from Lee et al. (2017)

The PDMS–PAN specimens contain no healing agent; thus, the crack length ℓ is a straightforward consequence of the external load σ_∞. As seen in Figs. 7.16, 7.17, 7.18, 7.19, and 7.20, crack propagation in the PRC specimens is delayed significantly and specimen failure occurs at a much larger strains, attributed to the presence of the liquid cores and the associated viscoelastic stress relaxation. The theory of Sect. 6.4 considers continuous crack propagation under the external load σ_∞, without considering the effect of the liquid cores. Furthermore, the fracture toughness K_{Ic} of the specimen also changes when considering the liquid cores. The theory of Sect. 6.4 is based on the calculation of K_{Ic} at the ultimate strength and assumes a homogeneous composite material throughout the crack propagation distance. Currently, no method exists for calculating or measuring K_{Ic} for the PDMS–PRC specimens. Thus, the theory of Sect. 6.4 cannot be compared to the observed crack propagation behaviors of the PDMS–PRC specimens.

References

Barenblatt GI (2014) Flow, deformation and fracture. Cambridge University Press, Cambridge

Cherepanov GP (1979) Mechanics of brittle fracture. McGraw Hill, New York

Coope TS, Mayer UFJ, Wass DF, Trask RS, Bond IP (2011) Self-healing of an epoxy resin using scandium (III) triflate as a catalytic curing agent. Adv Funct Mater 21:4624–4631

Coope TS, Wass DF, Trask RS, Bond IP (2014) Metal triflates as catalytic curing agents in self healing fibre reinforced polymer composite materials. Macromol Mater Eng 299:208–218

Feng L, Li S, Li H, Zhai J, Song Y, Jiang L, Zhu D (2002) Super-hydrophobic surface of aligned polyacrylonitrile nanofibers. Angew Chem Int Ed Eng 41:1221–1223

Heinamaki JT, Lehtola VM, Nikupaavo P, Yliruusi JK (1994) The mechanical and moisture permeability properties of aqueous based hydroxypropyl methylcellulose coating systems plasticized with polyethylene-glycol. Int J Pharm 112:191–196

Joffe R, Madsen B, Nattinen K, Miettinen A (2015) Strength of cellulosic fiber/starch acetate composites with variable fiber and plasticizer content. J Compos Mater 49:1007–1017

Khansari S, Sinha-Ray S, Yarin AL, Pourdeyhimi B (2012) Stress-strain dependence for soy protein nanofiber mats. J Appl Phys 111:044906

Khansari S, Sinha-Ray S, Yarin AL, Pourdeyhimi B (2013) Biopolymer-based nanofiber mats and their mechanical characterization. Ind Eng Chem Res 52:15104–15113

Kim M-S, Shin H-J, Park Y-K (2011) Measurement of nonlinear mechanical properties of PDMS elastomer. Microelectron Eng 88:1982–1985

Landau LD, Lifshitz EM (1986) Theory of elasticity. Reed Educational and Professional Publishing Ltd, Oxford

Leblanc JL, Furtado CRG, Leite MCAM, Visconte LLY, de Souza AMF (2007) Effect of the fiber content and plasticizer type on the rheological and mechanical properties of poly(vinylchloride)/green coconut fiber composites. J Appl Polym Sci 106:3653–3665

Lee MW, An S, Jo HS, Yoon SS, Yarin AL (2015) Self-healing nanofiber-reinforced polymer composites: 1. Tensile testing and recovery of mechanical properties. ACS Appl Mater Interfaces 7:19546–19554

Lee MW, Sett S, Yoon SS, Yarin AL (2016a) Self-healing of nanofiber-based composites in the course of stretching. Polymer 103:180–188

Lee MW, Sett S, Yoon SS, Yarin AL (2016b) Fatigue of self-healing nanofiber-based composites: static test and subcritical crack propagation. ACS Appl Mater Interfaces 8:18462–18470

Lee MW, Sett S, An S, Yoon SS, Yarin AL (2017) Self-healing nano-textured vascular-like materials: Mode I crack propagation. ACS Appl Mater Interfaces 9:27223–27231

Lim H, Hoag SW (2013) Plasticizer effects on physical–mechanical properties of solvent cast Soluplus® films. American Association of Pharmaceutical Scientists 14:903–910

Parton VZ, Morozov EM (1989) Mechanics of elastic-plastic fracture, 2nd edn. Hemisphere Publishing Corporation, New York

Sinha-Ray S, Khansari S, Yarin AL, Pourdeyhimi B (2012) Effect of chemical and physical cross-linking on tensile characteristics of solution-blown soy protein nanofiber mats. Ind Eng Chem Res 51:15109–15121

Sinha-Ray S, Yarin AL, Pourdeyhimi B (2014) Meltblown fiber mats and their tensile strength. Polymer 55:4241–4247

Standard Test Method for Determining Tensile Properties of Fiber Reinforced Polymer Matrix Composites Used for Strengthening of Civil Structures (2017) ASTM D7565/D7565 m-10. West Conshohocken, PA

Yarin AL, Pourdeyhimi B, Ramakrishna S (2014) Fundamentals and applications of micro- and nanofibers. Cambridge University Press, Cambridge